

# Crystal Structure of Tropomyosin at 7 Å Resolution

Frank G. Whitby and George N. Phillips, Jr.\*

Department of Biochemistry and Cell Biology, Rice University, Houston, Texas

**ABSTRACT** Tropomyosin is a 400Å-long coiled coil that polymerizes to form a continuous filament that associates with actin in muscle and numerous non-muscle cells. Tropomyosin and troponin together form a calcium-sensitive switch that is responsible for thin-filament regulation of striated muscle. Subtle structural features of the molecule, including non-canonical aspects of its coiled-coil motif, undoubtedly influence its association with f-actin and its role in thin filament regulation. Previously, careful inspection of native diffraction intensities was sufficient to construct a model of tropomyosin at 9Å resolution in a spermine-induced crystal form that diffracts anisotropically to 4Å resolution. Single isomorphous replacement (SIR) phasing has now provided an empirical determination of the structure at 7Å resolution. A novel method of heavy-atom analysis was used to overcome difficulties in interpretation of extremely anisotropic diffraction. The packing arrangement of the molecules in the crystal, and important aspects of the tropomyosin geometry such as non-uniformities of the pitch and variable bending and radius of the coiled coil are evident. *Proteins* 2000;38:49–59.

© 2000 Wiley-Liss, Inc.

**Key words:** alpha helix; coiled coil; muscle regulation; thin filament; tropomyosin

## INTRODUCTION

Vertebrate  $\alpha$ -tropomyosin is composed of two identical or highly homologous  $\alpha$  helices of 284 residues each. The helices associate in parallel and in register to form a 420Å-long coiled coil and polymerize head-to-tail along the actin filament. The length of each molecule is appropriate for it to span seven actin monomers. Tropomyosin, in association with troponin, forms a calcium-sensitive switch, which controls muscle contraction by inhibiting the interaction of myosin and actin. Relief of inhibition involves calcium-induced conformational changes in troponin and a change in the azimuthal position of tropomyosin on the actin filament, allowing the cooperative binding of myosin along the thin filament.

Sequence analysis of tropomyosin reveals an unbroken pattern of residues consistent with the coiled-coil motif. The coiled-coil, or leucine-zipper motif is increasingly recognized as an important element of numerous proteins where it typically stabilizes subunit associations. A well-studied example is the coiled-coil domain of the yeast

transcription factor GCN4 which was solved at high resolution and formed the basis for subsequent mutational and structural analyses that address the design of coiled coils.<sup>1</sup> Typical of coiled coils, the amino-acid sequence of tropomyosin has an unbroken repeating pattern of seven residues (*a-b-c-d-e-f-g*), where positions *a* and *d* are hydrophobic residues.<sup>2–4</sup> The non-integer nature of the pitch of the  $\alpha$  helix results in a hydrophobic stripe of residues that winds along the length of the helix, and thus two interacting helices wind gently around one another, forming a left-handed supercoil, or coiled coil.<sup>5,6</sup> Favorable salt bridges between residues *e* and *g* of adjacent helices likely stabilize the coiled-coil structure.<sup>2,3</sup>

The tropomyosin sequence also reveals a 14-fold periodic distribution of charged and nonpolar residues that has been related to its function as an actin-binding protein, forming actin-binding sites. These sites generally support the steric-blocking model of filament regulation.<sup>3,7,8</sup> Mutational analysis resulting in internal deletions of tropomyosin has also shown the importance of seven or fourteen periodic actin-binding sites on tropomyosin and has implicated some of the sites in contributing greater to the overall binding than others.<sup>9,10</sup>

Numerous other biophysical and structural studies support the general idea of the steric-blocking model of thin-filament regulation and have led to our current understanding of the role of tropomyosin in the thin filament. It has been estimated from time-resolved fiber diffraction of muscle fibers, for example, that tropomyosin movement precedes cross-bridge attachment by 12 to 17 ms,<sup>11</sup> but neutron scattering experiments suggest that tropomyosin does not move as a rigid rod, as there is apparently no change in the average radial position of tropomyosin on thin filaments.<sup>12</sup> X-ray diffraction from tropomyosin crystals has shown that it is very flexible, implying that local changes in its structure are important for muscle regulation and cooperative cross-bridge attachment.<sup>13,14</sup> Despite its flexible nature, electron micrograph

Grant sponsor: National Institutes of Health; Grant number: AM-32764; Grant sponsor: The Robert A. Welch Foundation; Grant number: C-1142; Grant sponsor: The W.M. Keck Center for Computational Biology; Grant number: NSF BIR-9413229; Grant sponsor: NIH Biophysics training grant; Grant number: GM-08280.

F.G. Whitby's present address is Department of Biochemistry, University of Utah School of Medicine, 50 N. Medical Drive, Salt Lake City, UT 84132.

\*Correspondence to: George N. Phillips, Jr., Department of Biochemistry and Cell Biology, Rice University, P.O. Box 1892, 6100 S. Main Street, Houston, TX 77005. E-mail: georgep@rice.edu.

Received 9 April 1999; Accepted 13 August 1999

(EM) reconstructions of decorated thin filaments suggest that tropomyosin occupies discrete azimuthal positions on the thin filament in the presence and absence of calcium,<sup>15</sup> and tropomyosin has been visualized occupying a position over residues on a model of F-actin thought to be directly responsible for cross-bridge attachment.<sup>16</sup> Refinements and reconstructions based on fiber diffraction data indicate that tropomyosin has a definite average position of rotation about its own axis and that it associates with actin entirely by electrostatic interactions.<sup>17</sup> Incorporation of the complete  $\alpha$ -tropomyosin sequence and the pitch of the coiled coil into these refinements was important in creating a realistic model of the unregulated thin filament.<sup>17</sup> Simulations of the overall behavior of the thin filament during regulation that include both structural and biochemical data seem to confirm the importance of cooperativity derived from actin-tropomyosin interactions.<sup>18</sup>

Because tropomyosin tends to form a wide variety of crystalline arrays under varying salt conditions, numerous low-resolution structural studies have been reported. Initial estimates of the structural parameters of the molecule were based on fiber diffraction studies, and notably, the pitch of the coiled coil was estimated to be about 186Å.<sup>19</sup> The structure was later determined at 15Å resolution in a relatively weakly diffracting crystal form.<sup>8,20</sup> This model was used to solve the structure by molecular replacement to a nominal resolution of 9Å in a crystal form that diffracts to greater than 4Å resolution.<sup>21,22</sup> From these structures, the pitch has been shown quite accurately to be about 140Å.<sup>8,22,23</sup>

The crystal structure of tropomyosin in both of these crystal forms has been determined thus far by non-standard methods and careful inspection of the diffraction data. In order to extend the structure of tropomyosin in the strongly-diffracting spermine-induced crystal form to the limit of resolution and to obtain an empirical determination of phases, heavy-atom derivatives have been sought and one has been solved. Difficulties in analyzing the highly anisotropic data from these crystals necessitated a novel, qualitative approach to determine the locations of the heavy atoms. SIR phase information has been used to build a more detailed model of tropomyosin at 7Å resolution. Important aspects of intermolecular contacts and the orientations of the molecules in the crystal have been determined. These features have been related to recent models of thin filament regulation and to the packing of molecules in spermine-induced paracrystals.

## RESULTS

Native and pre-reacted mercury-derivative tropomyosin molecules crystallized in space group C2 with unit cell parameters  $a=259.7$ ,  $b=55.3$ ,  $c=136.3$ ,  $\beta=97.4^\circ$  (Table I). The anisotropic distribution of diffraction is characteristic of a fibrous structure, and the localization of strong diffraction maxima to specific regions of reciprocal space clearly indicates the localization of levels of structural detail (Fig. 1). The transform to about 7Å resolution is dominated by the paths of the molecules through the unit

TABLE I. Data Collection Statistics

|                                   | Native <sup>a</sup> | Thimerosal <sup>a</sup> |
|-----------------------------------|---------------------|-------------------------|
| # Observed Refls                  | 30004               | 9484                    |
| # Unique Refls                    | 10193               | 2931                    |
| dmin (Å)                          | 4.0                 | 7.0                     |
| Completeness (%)                  | 90.2                | 97.1                    |
| R <sub>sym</sub> <sup>b</sup> (%) | 8.3                 | 5.8                     |

<sup>a</sup>Data collected at BNL beamline X8C using CCD detector.

<sup>b</sup>R<sub>sym</sub> =  $100 * \sum |I - \langle I \rangle| / \sum I$ .

cell, their relative orientations, and other low-resolution features of the molecules themselves, such as the pitch of the coiled coil and supercoiling of the molecules. The transform in the 5Å meridional region is dominated by the internal structure of the  $\alpha$  helices, side-chain conformations, and the average pitch of the  $\alpha$  helices in projection. The data beyond 5Å resolution are dominated by the transform of the amino-acid sequence and the side-chain interactions of the coiled coil. As previously noted,<sup>22</sup> another striking feature of the diffraction is the strong sinusoidal fringe function that can be seen in the ( $h0l$ ) plane of reciprocal space. The inter-node spacing of the fringe function is about 44Å. This indicates that the molecules are packed in sheets or layers with an inter-layer separation of about 22Å and that the molecules lie in sheets parallel to the ( $40\bar{6}$ ) plane of reciprocal space.<sup>21,22</sup> The molecules polymerize head-to-tail to form continuous filaments running through the crystal and this fixes their directions to be integer multiples of the unit cell. Arcs of diffraction in the ( $0kl$ ) and ( $h0l$ ) views indicated that the molecules run essentially parallel to the (332) and symmetry-related ( $3\bar{3}2$ ) directions.<sup>21,22</sup> These details, obtained by inspection of the native diffraction intensities, allowed for the construction of a model that accurately describes the structure at 9Å resolution.<sup>22</sup>

To circumvent the lack of isomorphism caused by soaking crystals in heavy-atom solutions, mercurials were reacted with protein prior to crystallization. A series of non-reducing sodium dodecyl sulfate polyacrylamide gel electrophoresis (SDS-PAGE) experiments demonstrated complete reactivity of cysteine 190 (there is one cysteine at position 190 on each helix) with thimerosal, and disulfide bond formation could not be induced in protein from dissolved derivative crystals (Fig. 2). X-ray-fluorescence confirmed the incorporation of mercury into the crystals. The position of the L<sub>III</sub> edge was the same for each of several crystals and was at the expected energy for elemental mercury (data not shown).

Inspection of pseudo-precession plots of the native and derivative data sets at 7Å resolution revealed large, obvious intensity changes for many reflections (compare Fig. 1a–c with Fig. 1d–f), leading us to believe that isomorphous phase information could be derived from these data. Unfortunately, initial isomorphous difference Patterson maps and difference Fourier maps calculated with phases from the 9Å structure were uninterpretable, suggesting a problem of scaling of the data sets. The anomalous signal of a 4-wavelength multiple-wavelength anomalous disper-

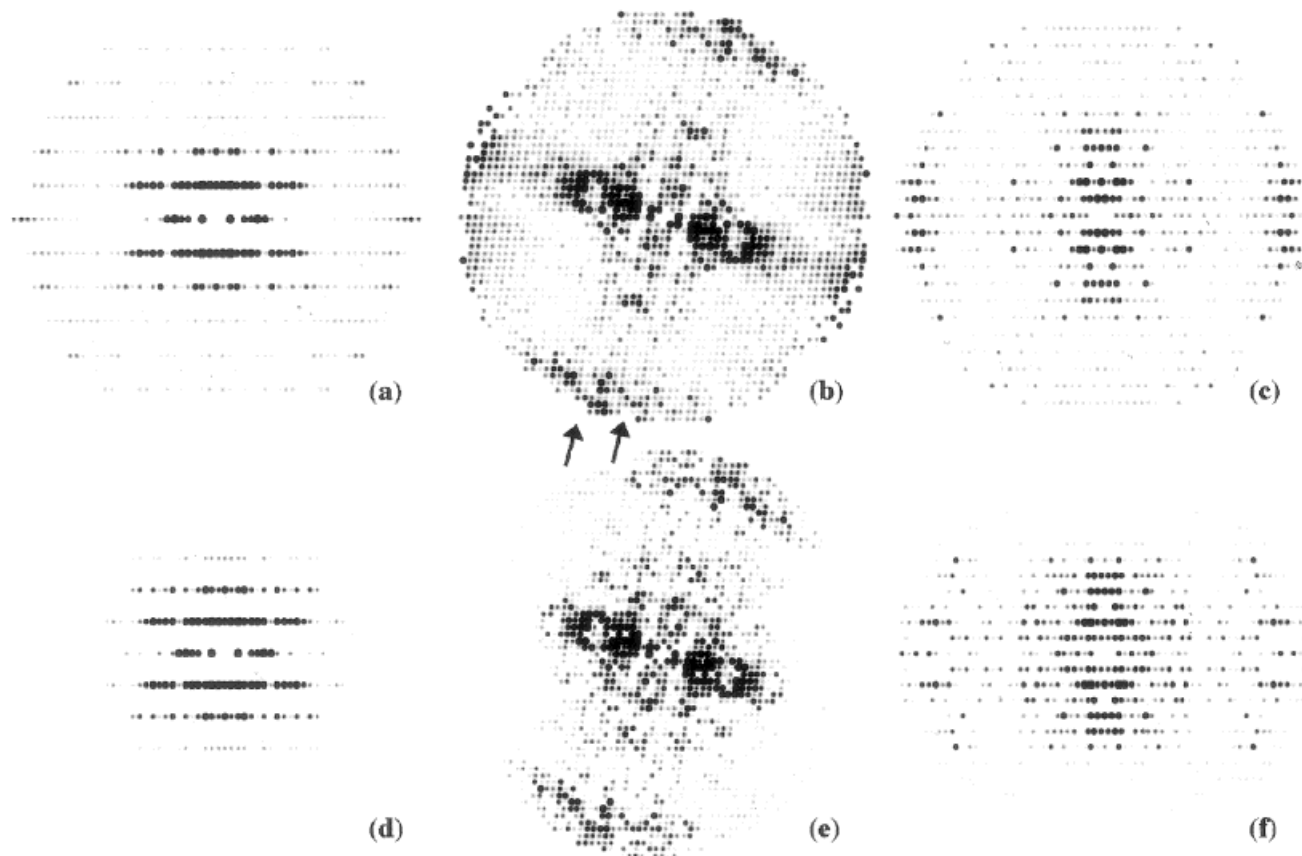


Fig. 1. Pseudo-precession plots of the measured X-ray diffraction intensities from native (a, b, c) and mercury-derivative (d, e, f) spermine-induced tropomyosin crystals for the three principal planes of reciprocal space. a) & d) ( $0kl$ ); b) & e) ( $h0l$ ); c) & f) ( $hk0$ ). The limit of diffraction shown in these plots is  $4.5\text{\AA}$ . The sinusoidal fringe function is apparent in the ( $h0l$ )

views. Significant intensity differences, arising from the added mercury atoms, are apparent, particularly in the ( $h0l$ ) view. The high anisotropic B-factor and obvious strong fall-off in overall diffraction intensity beyond  $7\text{\AA}$  resolution in the equatorial direction seen in panel (e) suggests that the mercury derivative crystal is more highly disordered than the native.

sion (MAD) data set was determined to be too weak to be of any use. The weakness of the anomalous signal was attributed to the high overall anisotropic B-factor of the data.

A qualitative examination of pseudo-precession-like plots of the calculated difference intensities ( $I_{\text{heavy}}$ ), revealed a strong scale-factor-independent sublattice extending to about  $7\text{\AA}$  resolution in the ( $h0l$ ) plane of the difference intensity plots (Fig. 3b). The sublattice indicated a real-space distribution of the mercury atoms on an  $18 \times 22\text{\AA}$  lattice where the  $22\text{\AA}$  spacing corresponds both in magnitude and direction to the sinusoidal fringe function that represents the inter-layer spacing of molecules.<sup>21,22</sup> The  $18\text{\AA}$  sublattice spacing perpendicular to the fringe function indicates that, viewed in projection, parallel to the b-axis (the centric zone), mercury atoms lie along the direction of the molecular layers, spaced  $18\text{\AA}$  apart, close to either a crystallographic two-fold or two-fold screw axis. The sublattice was simulated by placing point scatterers in the unit cell representing the positions of mercury atoms (Fig. 3a).

Based on the distribution of values in the difference intensity plots, the data sets were manually rescaled to achieve a relatively even distribution of positive and negative difference intensities ( $I_{\text{heavy}}$ ).

The resulting difference Patterson maps were readily interpretable, confirming the sublattice analysis, and indicating that the two mercury pairs of the asymmetric unit are separated by  $1/3$  of the unit cell parallel to the b-axis. This is consistent with the  $9\text{\AA}$  structure,<sup>22</sup> in which the intra-layer separation between the two molecules of the asymmetric unit was shown to vary along the length of the molecule.

An  $F_o$  map, calculated using only SIR, experimental phase information shows clear molecular layers with a spacing of  $22\text{\AA}$  running parallel to the ( $406$ ) direction (Fig. 4). This map provides independent evidence for the validity of the  $9\text{\AA}$  structure. A  $2F_o - F_c$  map, calculated using partial phase information from the  $9\text{\AA}$  structure and the derivative data, shows clearly the two  $\alpha$ -helical strands of the molecule (Fig. 5). The spacing and run of the filaments coincide closely with the  $9\text{\AA}$  structure.

The positions of the molecular ends were determined relative to the Cys-190 residues, whose positions were fixed by the solution of the mercury-pair positions. An idealized poly-alanine  $\alpha$ -helical molecule was built and broken into 19 segments of 28 residues each (14 residues per helix) and one segment of 36 residues. Rigid-body and



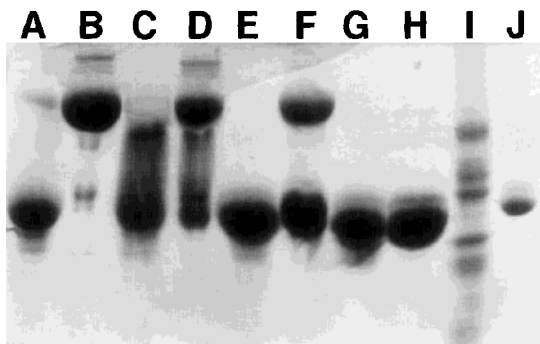


Fig. 2. Coomassie-stained non-reducing SDS-PAGE showing that mercury protected the cysteine-190 residues of tropomyosin from being oxidized to a disulfide bond. Following reaction with a mercury compound, oxygen was bubbled through the sample, either in the presence or absence of  $\text{CuCl}_2$ , to try to promote disulfide bond formation. Native, reduced tropomyosin has a molecular weight of about 33,000 Daltons indicated by a single strong band in lane (J), which contains the purified protein. Molecular weight standards (Sigma Chemicals) are shown in lane (I). Lane (A) native protein ( $-\text{CuCl}_2$ ). Lane (B) native protein ( $+\text{CuCl}_2$ ). Lane (C) protein reacted with mercuri-nitrophenol (MNP) ( $-\text{CuCl}_2$ ). Lane (D) protein+MNP ( $+\text{CuCl}_2$ ). Lane (E) protein+PCMBs ( $-\text{CuCl}_2$ ). Lane (F) protein+PCMBs ( $+\text{CuCl}_2$ ). Lane (G) protein+thimerosal ( $-\text{CuCl}_2$ ). Lane (H) protein+thimerosal ( $+\text{CuCl}_2$ ). Lanes (A) and (B) demonstrate that in the presence of a trace amount of  $\text{CuCl}_2$ , oxygen strongly promotes disulfide bond formation between the helices of native tropomyosin. Partial dimer formation in lanes (D) and (F) indicate that MNP and PCMBs did not react fully with the Cys-190 residues. Lane (H) shows that under strongly oxidizing conditions thimerosal fully blocks dimer formation.

overall B-factor refinement were carried out allowing all of the segments to move independently. Four alternative models were refined, corresponding to the four possible relative orientations of the two molecules of the asymmetric unit. Four additional refinements were carried out with models incorporating the sequence of tropomyosin. Following four cycles of refinement of the antiparallel choice-1 model, the crystallographic R-factor dropped from 55% to 40.4% (Table II). The correlation coefficient increased from 0.90 to 0.99 (target function F2F2 in XPLOR). The R-factor was 33.6% for all data to  $7\text{\AA}$  with  $I/\sigma I > 10$ . Refinement resulted in significant movements of some of the segments, but the molecules clearly remained intact and were not fragmented. Although the crystallographic R-factor appears poor by high-resolution standards, this is a reasonable fit considering the anisotropic nature of the data and the rough nature of the model. Attempts to improve the quality of the solutions with group B-factor refinement, a bulk solvent mask and manipulation of the scattering factors to account for variations in scattering factors at low resolution did not improve the results. Constrained positional refinement was used to "anneal" the segments of the model together and form a single filament. The resulting model represents a more stereochemically reasonable model of tropomyosin.

The results of the refinements strongly suggest that the two molecules in the asymmetric unit are antiparallel, with their C-terminal ends overlapping by about 2/3 of the molecular length. The refinement was sensitive to slight changes in the initial choice of the head-to-tail overlap

positions. Because these positions are fixed relative to the position of Cys-190, this suggests that the antiparallel choice-1 of the two molecules in the asymmetric unit is correct.

Clearly defined coiled coil can be seen along most of the length of the molecules (Fig. 5). The interactions of the molecules in adjacent layers are not regular and are affected by the angle at which the molecules in adjacent layers cross. This crossing angle is about  $20^\circ$ , but varies due to the curvature of the molecules within the layers. Extra density is visible where the molecules polymerize end-to-end, but details of the overlap cannot be determined at this resolution. The density of the molecules in the region adjacent to the head-to-tail overlaps is less well defined. The polymerization of one filament might cause local disorder in the neighboring filaments, resulting in weaker electron density in that region of the map. The separations between molecules is small compared to the diameter of the filaments themselves. Along part of the path of the molecules, shown in the center-right of Figure 5, the two molecules of the asymmetric unit appear to form a closely associated pair separated by about  $20\text{\AA}$ , while the separation between adjacent molecules is several angstroms greater. The molecules follow a sinusoidal path through the crystal and in some regions neighboring molecules are staggered by an odd number of quarter pitches, but in others the stagger is obviously not so regular. The C-termini of the molecules overlap axially by about 2/3 the molecular length. Each molecule makes contacts with six neighboring molecules within a layer. Two of these contacts are end-to-end polymerization contacts and four are side-by-side associations.

Omit maps indicated the correctness of the model. In the case where an entire molecule was omitted from the calculation, the map showed clearly that a second molecule lay near the existing one and that it ran nearly parallel to it. Omit maps made while omitting the N- and C-terminal 20-residue polymerization regions had clear density at these positions. The density did not, however, reveal any additional structural information.

## DISCUSSION

The approximate packing arrangement of molecules in the spermine-induced crystal form was previously determined at  $9\text{\AA}$  resolution by molecular replacement and specialized refinement of a simplified atomic model.<sup>22</sup> The solution of a single mercury derivative has provided an empirical determination of phases and a more detailed model that accounts for the directionality of the filaments in the crystal. The remarkably anisotropic diffraction from these crystals necessitated careful inspection of diffraction intensities, leading to a novel solution of a mercury derivative. The success of this approach indicates the importance of careful re-examination of diffraction intensities when conventional heavy-atom analysis fails.

Refinement of the structure at  $9\text{\AA}$  resolution demonstrated that the average pitch of the coiled coil is about  $140\text{\AA}$ .<sup>22</sup> Variations in the pitch of the coiled coil are evident in the electron density map at  $7\text{\AA}$  resolution (Fig. 5) and

are probably due to local sequence variations. The pitch is dependent upon the long-range regularity of the heptad repeat and supercoiling of the molecule. The pitch is locally shortened near the head-to-tail overlap (right-center in Fig. 5, Fig. 6). This is in a relatively tight bend of the molecule, and although it is possible that the bend is an inherent feature of tropomyosin, crystal packing forces are probably sufficient to deform the molecule, as tropomyosin has low flexural rigidity.<sup>13,24,25</sup>

The radius of the coiled coil is sequence-dependent, although in the present refinement the distance between the two helices was constrained. The axes of the  $\alpha$  helices of engineered leucine zippers are separated by about 9.3 to 9.8 Å and the preference for isoleucine, leucine, and valine residues at core positions correlates with variations in the radius.<sup>1,26–30</sup>

Spermine probably promotes layer formation by bridging the distance between charged actin-binding zones on adjacent molecules. One molecule crosses over molecules in the adjacent layers six times, leading to inter-sheet contacts about every 58 Å along the molecule.

Because the C-termini overlap by about two-thirds of the molecular length, the extra density of the head-to-tail polymerization regions divides the asymmetric unit approximately into thirds when viewed normal to the broad flat face of the crystals (the 406 plane). This axial division is similar to the banding pattern seen in micrographs (Fig. 7) of  $Mg^{+2}$ -paracrystals,<sup>31–38</sup> and spermine-induced microcrystals.<sup>22,39,40</sup> This “thirding” matches the microcrystal pattern precisely if two layers of molecules are stacked exactly as they are in the X-ray crystal. Adding more layers of molecules eventually creates a continuum of bands, indicating that the spermine-induced microcrystals are either only two molecules thick or that their organization beyond two layers of molecules differs from the X-ray crystal packing. There is a high degree of variability in the microcrystal packing, yet all of the microcrystalline and paracrystalline forms are probably closely related.

The azimuthal relationship of tropomyosin to actin is clearly very important,<sup>10,17,41</sup> and the structure of the head-to-tail overlap may affect the azimuthal disposition of the actin binding zones. The current structure does not accurately describe the overlap regions, but the small “blocks” of coiled-coil used in the rigid-body refinement allowed the end segments of the molecules to rotate

axially. One of the molecules has no abrupt change in the coiled-coil phase over the entire length of the filament, while the other appears to have a coiled-coil phase shift of about 90 degrees at the overlap. A two-site model of steric blocking where the  $\alpha$  sites are bound in the “off” state and the  $\beta$  sites are used in the “on” state<sup>7</sup> would favor a continuous model of tropomyosin with no azimuthal phase shift of the polymerized filament. If, on the other hand, the ends of the molecules associated with a 90° phase shift, the azimuthal relationship of every second molecule with respect to actin would be identical, but 90° phase-shifted from that of the intervening molecule. This would create a pair-wise interaction of tropomyosin with actin (K. Holmes, personal discussion). In this case, binding interactions in both rigor and blocking states would be expected to be quite similar and the model of Lorenz et al.<sup>17</sup> would predict that every other molecule would be in a less than ideal orientation. The geometry of polymerization is an important feature of tropomyosin and further improvements in resolution should allow an accurate description of the overlap in the spermine-induced crystal.

## SUMMARY

Tropomyosin is the archetypal coiled-coil molecule. The almost uninterrupted heptad of hydrophobic side chains suggests a highly regular molecule. Although not yet visualized in detail, our results show that the molecule is not highly regular in all respects, but has degrees of irregularity as well. The importance of these deviations is, and will continue to be difficult to establish, but new interactions of tropomyosin continue to be found. It is tempting to speculate that the surface of tropomyosin has more to its function than regular attachment to actin and troponin. The high degree of isoform diversity of tropomyosins from many sources<sup>42,43</sup> likely results in subtle structural changes to the coiled coil, which, when extended over the length of the molecule, influence the activity of the combined regulatory mechanisms.

Analysis of the packing of tropomyosin in various aggregated forms, including crystals, continues to provide strong evidence for head-to-tail linked polymers, which is a central assumption in ideas about the interaction of tropomyosin with actin. Results like those presented here allow more extensive interpretation of electron microscopic images, and thus improve our knowledge of structure in the complex assemblies that form the thin filament of muscle.

Fig. 3. (Overleaf). A comparison between observed and simulated difference intensity distributions. **Left:** The (*h*0) plane of the simulated intensity distribution from the 2-atom mercury-pair model. **Right:** The (*h*0) plane of a pseudo-precession-like plot of mercury-minus-native difference intensities. Positive difference intensities are shown in red, negative ones in blue. The magnitude of each difference intensity is proportional to the brightness of the spot. Difference intensities with a very small absolute value blend into the black background. The data are shown to a limit of 7 Å resolution in each plot. The simulated sublattice spacing in panel a matches well with that of the observed sublattice in panel b.

Fig. 4. (Overleaf). SIR-Fo map calculated at 7 Å resolution, viewed in projection parallel to the b-axis. Very clear layers of molecules are visible. The empirical determination of phases from the mercury derivative confirms the molecular packing determined previously at 9 Å resolution.

Fig. 5. (Overleaf). 2Fo-Fc map following refinement of the atomic model at 7 Å resolution. The b-axis is oriented vertically in this view. One layer of molecules is shown to illustrate the tight side-by-side packing geometry in the spermine-induced crystal form. Ribbon diagrams of the two molecules of the asymmetric unit of the antiparallel choice-1 model are shown superimposed on the map (one in yellow, one in blue). Regions of extra density are visible at the head-to-tail polymerization positions (the ends of the molecules). The molecules follow a sinusoidal path through the crystal with only small, but variable separations between filaments. The geometry of interactions between neighboring molecules within the layers varies along their length. In addition, the pitch of the coiled coil can be seen to vary along the length of a molecule.



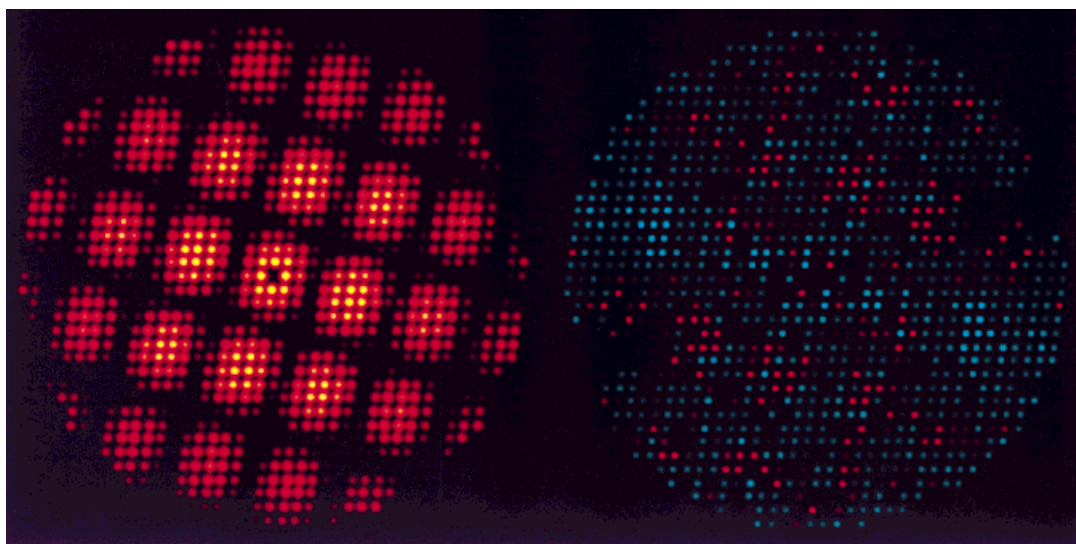


Figure 3.

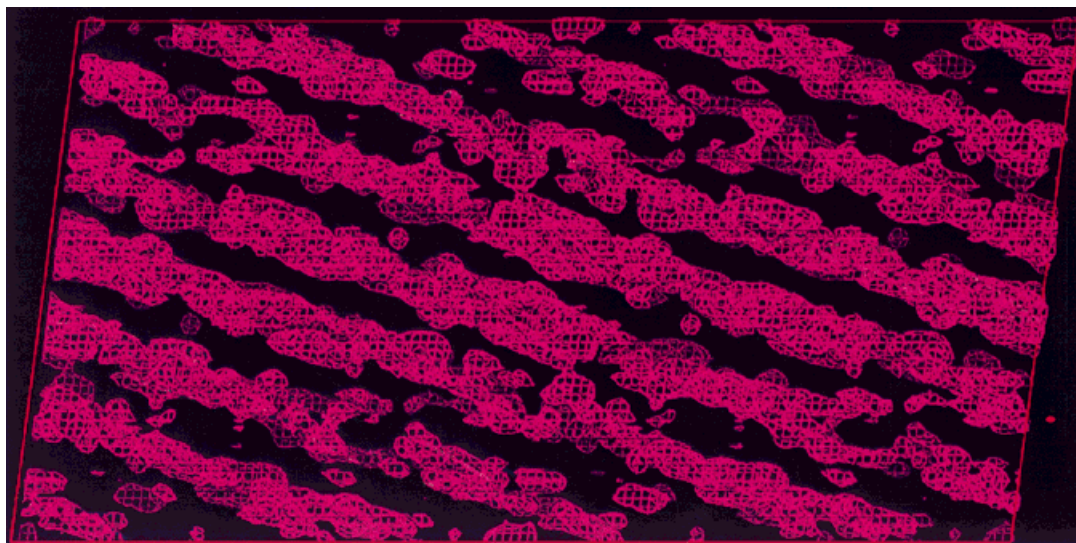


Figure 4.

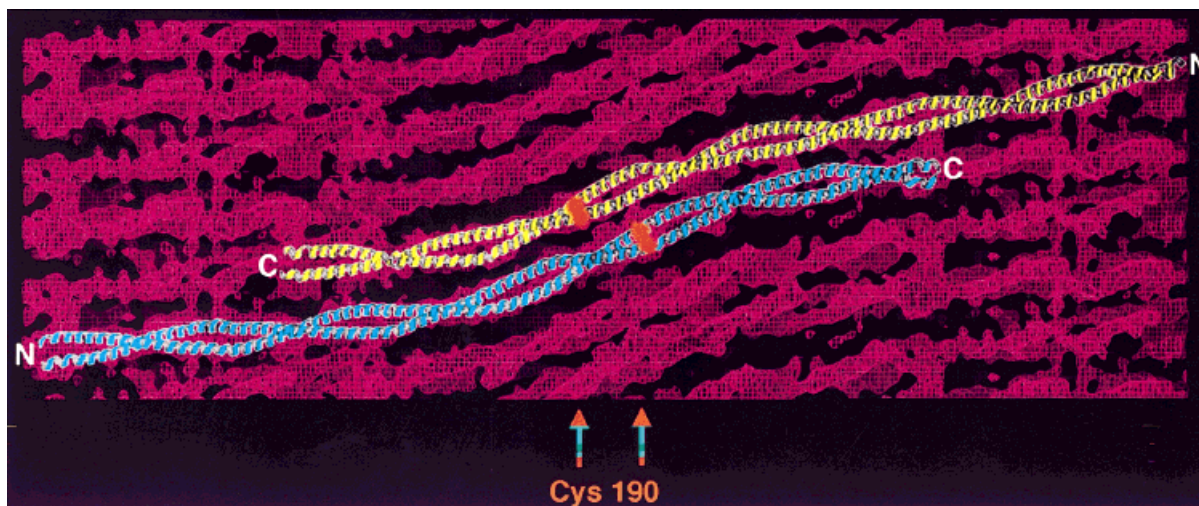


Figure 5.

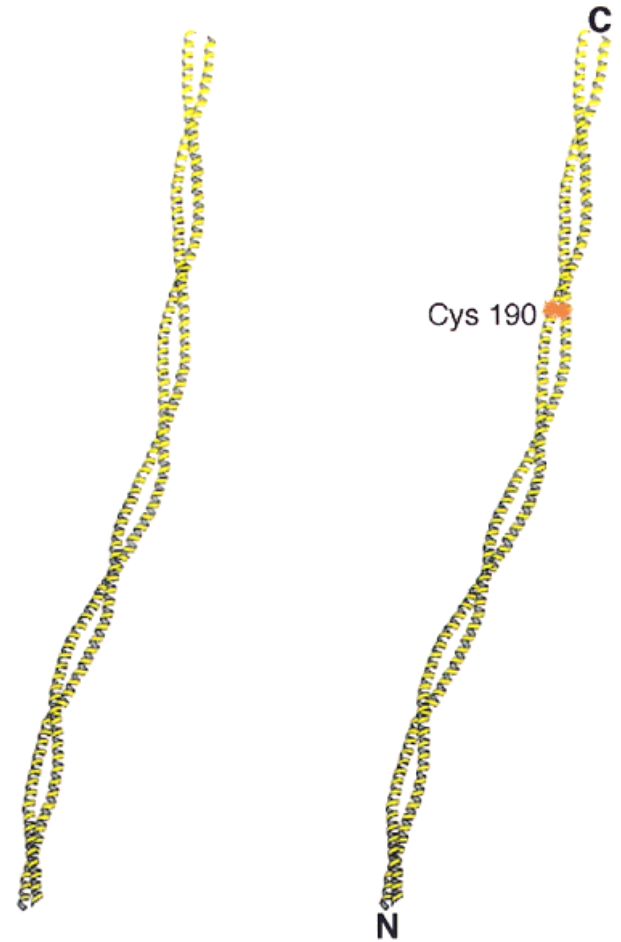


Fig. 6. (Right.) A stereoscopic plot of the coordinates of one of the tropomyosin coiled coils in the asymmetric unit. The gentle bending is similar that seen in the Bailey crystal form of tropomyosin, but the current analysis yields local variation in the bending angles and radius.

Fig. 7. (Below.) Comparison of the packing of tropomyosin molecules in the X-ray form of spermine-induced tropomyosin crystals and the microcrystals studied by cryo-electron microscopy. For clarity, two layers of molecules from the X-ray structure, related by the crystallographic operators, are shown above and below the micrograph section. The singlet-singlet-doublet banding pattern observed in the microcrystals is matched by the alignment of the end-to-end overlaps of molecules in two layers of the spermine-induced crystals.

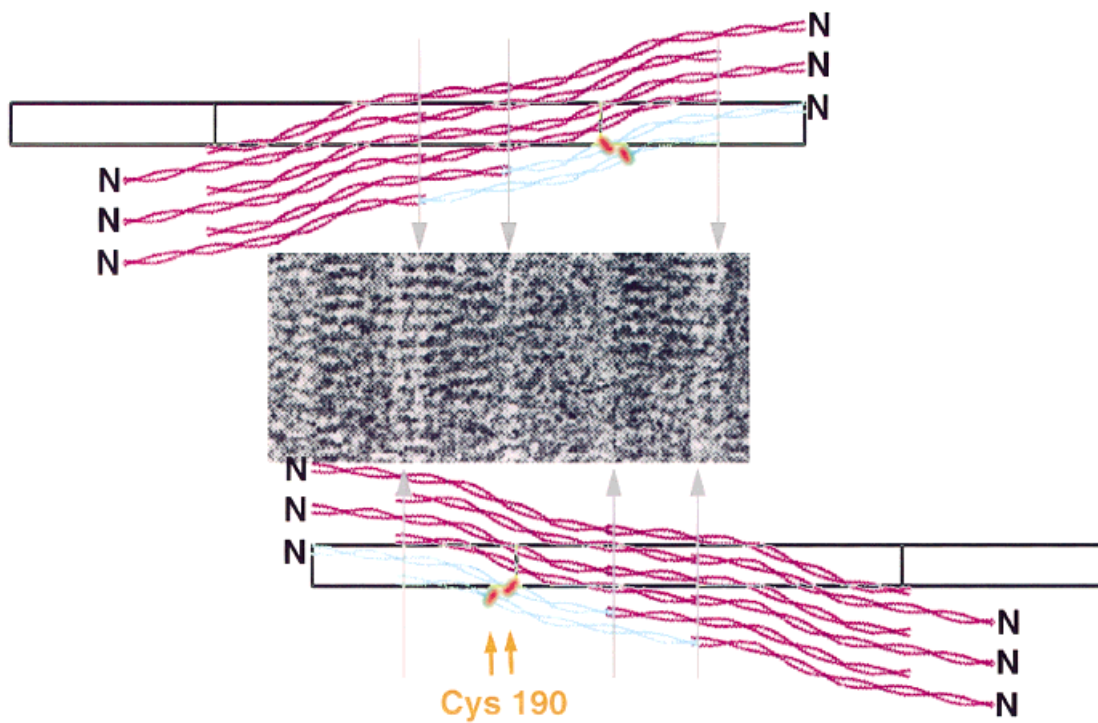


TABLE II. Refinement Statistics

|                           | Antiparallel<br>choice-1 | Antiparallel<br>choice-1 | Antiparallel<br>choice-2 | Parallel<br>choice-1 | Parallel<br>choice-2 |
|---------------------------|--------------------------|--------------------------|--------------------------|----------------------|----------------------|
| Resolution range (Å)      | 100.0–7.0                | 100.0–7.0                | 100.0–7.0                | 100.0–7.0            | 100.0–7.0            |
| Atoms included            | all                      | poly-alanine             | all                      | all                  | all                  |
| R-factor (%) <sup>a</sup> | 40.4 (33.6)              | 49.1                     | 46.3                     | 47.3                 | 47.9                 |
| <B> (Å <sup>2</sup> )     | 210.0                    | 414.7                    | 183.8                    | 148.0                | 150.1                |

<sup>a</sup>R-factor =  $100 \times \Sigma(|F_p(\text{obs})| - |F_p(\text{calc})|) / \Sigma |F_p(\text{obs})|$ . All data were used in the resolution range indicated, without application of a cutoff based upon the estimated standard deviation. The value in parentheses is based on a cutoff of 10 times the estimated standard deviation of the data.

Our results also show that progress can be made in determining the structures of difficult molecules by careful application of knowledge about diffraction, and that aspects of fiber diffraction and crystallography can be combined to yield better results than can either technique alone.

## MATERIALS AND METHODS

Alpha-alpha tropomyosin was prepared from adult porcine ventricles (Pel-Freez Biologicals) and crystallized in a buffer containing spermine as previously described.<sup>20,22,44</sup> Briefly, purified, lyophilized tropomyosin was dialyzed in dissolving buffer (0.6M KCl, 1.0 mM DTT, 1.0 mM EDTA, 50 mM Tris-base, pH 8.0). The protein sample was then dialyzed in pre-crystallization buffer (DBC2) (1.0 mM EDTA, 1.0 mM DTT, 1.0 mM Tris-base, pH 8.0). The sample was then dialyzed in concentrated spermine buffer (2MSP) made by adding spermine-HCl (Sigma Chemicals) to DBC2 to a final concentration of 200 mM. This concentrated buffer was then diluted to 70 mM spermine (7MSP) by adding additional DBC2, and further dialysis was performed. The protein sample, initially containing 20 to 30 mg/ml tropomyosin at 70 mM spermine, was then placed in capillaries, open at one end, containing low-spermine buffer for crystallization by liquid diffusion.<sup>45</sup> As the spermine concentration dropped to around 40 to 65 mM spermine, plate-like crystals occasionally grew in several weeks with typical dimensions of 1.5 mm × 1.0 mm × 0.5 mm.<sup>22</sup>

Non-reducing SDS-PAGE experiments indicated that 20 mM DTT is adequate to ensure full reduction of the sulfhydryls of tropomyosin. To test our ability to quantitatively oxidize the cysteine residues to a disulfide bond, a sample of tropomyosin was dialyzed for 6 hours at 4° C in DBC2 containing 20 mM DTT (DBC2<sup>(+20DTT)</sup>) to ensure that the cysteines were fully reduced. This step was repeated once. The sample was then dialyzed twice for 6 hours each time at 4° C in DBC2 containing no DTT (DBC2<sup>(-DTT)</sup>). The concentration of the sample was checked and the sample was diluted to 10 mg/ml protein with the dialysis buffer. The sample was divided into three parts. One third was placed in a vial, sealed with a rubber septum, and a needle was used to bubble oxygen gas through the solution for 5 minutes. The sealed vial was left to sit overnight at 4° C. One third was treated in a manner similar to the first except that nitrogen was bubbled through the solution in the place of oxygen. The remaining

third of the sample was placed in a similar vial, sealed, and left to sit overnight without further treatment. Non-reducing SDS gel samples were then prepared and the three samples were run on a non-reducing SDS-PAGE. Based on the migration of protein bands at the level of a monomer and a dimer, this test indicated that exposing the sample to oxygen in this manner was sufficient to oxidize only about half of the protein to its disulfide bonded state. Thus, a fresh sample of tropomyosin was prepared by the same series of dialysis steps just described. The sample was then divided into six parts. Three parts were treated in the same manner as just described. The other three parts were treated in this way also, except that prior to placing each portion of the tropomyosin solution in the vial, a small amount of CuCl<sub>2</sub> in deionized water was added to a final concentration of 0.1 mM. The results of a non-reducing SDS-PAGE using these samples indicated that complete oxidation of the cysteines could be induced by addition of CuCl<sub>2</sub> in the presence of oxygen.

Mercury-reacted samples of tropomyosin were then tested to see if mercury prevents disulfide bond formation under strongly oxidizing conditions.<sup>35,46</sup> A fresh sample of fully-reduced tropomyosin in non-reducing buffer was prepared by the series of dialysis steps described above. The fully reduced sample was then dialyzed overnight at 4° C in DBC2<sup>(-DTT)</sup> containing 10 mM of one of several mercury compounds. The sample was then dialyzed twice in 200 ml fresh DBC2<sup>(-DTT)</sup> to remove excess mercury. The sample was diluted to 10 mg/ml and divided into five parts. One sample was placed in a sealed vial and allowed to stand overnight at 4° C without further treatment. Two of the samples were placed in vials and either oxygen or nitrogen was bubbled through them for 5 minutes. Each vial was then sealed and allowed to stand overnight at 4° C. The remaining two samples were bubbled with oxygen or nitrogen following the addition of CuCl<sub>2</sub> to a final concentration of 0.1 mM. Gel samples were prepared from each of the five protein samples and these were run on a non-reducing SDS-PAGE.

Crystals grown from protein that had been pre-reacted with either thimerosal or *p*-chloromercuribenzyldisulfonic acid (PCMBs) were dissolved in a small volume (20 µl) of dissolving buffer containing no DTT (0.6M KCl, 1.0 mM EDTA, 50 mM Tris-base, pH 8.0). The sample was dialyzed at 4° C for 4 hours in DBC2<sup>(-DTT)</sup> and then transferred to a small vial. CuCl<sub>2</sub> was added to 0.1 mM, oxygen was bubbled through the solution for 5 minutes, the vial was



sealed, and the solution was allowed to sit overnight at 4° C. A gel sample was then prepared from the protein and it was run on a non-reducing SDS-PAGE.

A few modifications were made to the native protein crystallization procedure in order to produce pre-reacted mercury derivative crystals. Following the initial dialysis of the protein sample in 300 ml DBC2, the sample was dialyzed overnight in 200 ml DBC2<sup>(+20DTT)</sup>. The sample was then dialyzed twice in 200 ml DBC2<sup>(-DTT)</sup>. The sample was then dialyzed in 25 ml DBC2<sup>(-DTT)</sup> containing a mercury compound at 10 mM. The container was tightly sealed and allowed to stand at 4° C for at least 8 hours. The dialysis tubing, containing the sample, was rinsed briefly (15 seconds) in 200 ml fresh DBC2<sup>(-DTT)</sup>. The sample was then transferred to 25 ml 2MSP containing no DTT (2MSP<sup>(-DTT)</sup>) at 4° C. After at least 8 hours, the sample was again rinsed briefly in 200 ml DBC2<sup>(-DTT)</sup> and transferred to 50 ml fresh 7MSP containing no DTT (7MSP<sup>(-DTT)</sup>) at 4° C. After 8 hours, the sample was again briefly rinsed in 200 ml fresh DBC2<sup>(-DTT)</sup> and transferred to 143 ml 7MSP<sup>(-DTT)</sup> and dialyzed at 4° C overnight. Following dialysis, the sample was centrifuged for 10 minutes at high speed in a microcentrifuge to remove insoluble debris and dust. Crystallization of mercury-derivative crystals was carried out in the dark in capillaries under conditions similar to those used for crystallizing native tropomyosin.

For in-house data collection, a Siemens X-ray generator was used to produce X-rays for use with a Siemens multi-wire area detector. A 0.3-cm × 3-cm fine-focus filament was used at 50kV and 90mA. The port was equipped with Franks double-focusing mirrors, which were optimized for the proper data collection geometry. Crystal-to-detector distance was typically 140 mm and a helium tunnel was used to reduce air scattering of the diffracted rays. Special effort was made to collect the low order reflections. This was accomplished by suspending a very small lead beam stop on a mylar strip close to the detector surface. Typically 400 to 500 rotation frames of 0.4° to 0.5° each were collected for 90 to 300 seconds each at room temperature (about 18° C).

Data were processed using the program XDS.<sup>47</sup> Several parameters were modified in order to facilitate indexing and profile fitting. RMIN, the variable that determines the minimum resolution for acceptable reflections, was changed from the default 50Å to 100Å. RMAX and RMAX1, the variables that determine the outer limit (radius) of the detector surface for accepting reflections, were frequently reduced from the default 260 & 265 pixels respectively to less than 200 pixels each as the situation demanded. DELPHI, the variable that determines the angular range over which reflections are gathered for profile averaging was commonly increased from the default 2.5° to 5.0° or more. Data quality was reduced by increasing DELPHI beyond 5.0°, but frequently this was a strong determining factor in facilitating processing. Multiple data sets were scaled using the program XSCALE.<sup>47</sup>

Native and derivative data were collected at the Brookhaven National Laboratories (BNL) synchrotron using a CCD-based detector system housed at beam line X8C

equipped with a four-circle goniometer (Table I). Three detector distances from 225 to 450 mm were used and several hundred 5- to 10-second rotation frames of 0.2° to 0.5° each were collected. A helium tunnel was not used. Data were processed with the program MADNES (Pflugrath & Kabsch). The data were scaled to other data sets with XSCALE.<sup>47</sup>

The mercury-derivative data set collected at BNL lacked many of the strong reflections below 15Å resolution because of saturation of the strong reflections on the CCD detector. Thus, additional low-resolution thimerosal-derivative data were collected in-house. Only the well-determined ( $I/\sigma I > 3$ ), low-resolution reflections from the resulting 15Å data set were merged with the data from BNL to produce a derivative data set that was more complete at low resolution and included the 406 reflection.

X-ray fluorescence spectra were measured from mercury-derivative crystals at beam line 1–5 at SSRL. Each mercury-derivative crystal was mounted in a glass capillary for data collection and placed on the goniometer in the path of the X-ray beam and scanned prior to data collection. An X-ray fluorescence detector was positioned at right angles to the incident radiation, about 1 cm from the crystal. The crystal was exposed to the X-ray beam while the beam-line monochromator was adjusted to scan through the desired range of energies. The X-ray fluorescence spectrum was recorded during the scan. The scan range and scan speed were adjusted to provide fine sampling in the region of the mercury L<sub>III</sub> absorption edge. The scan was repeated for different orientations of the crystal, but no orientation-dependent difference in the absorption edge was seen.

Wavelengths were chosen for MAD data collection based on the X-ray fluorescence energy scan. Anomalous scattering factors were determined from X-ray absorption spectra with the aid of the program DISCO (K. Eichorn & P. Phizackerly, SSRL).<sup>48</sup> Analysis of the diffraction data was performed with the MADSYS set of analysis programs.

An initial estimate of the scale factor (K) between derivative and native data sets to 7Å resolution was determined with the program XSCALE. The scale factors K and B are applied by XSCALE to each data set according to the equation  $K \cdot \exp(B/SS)$ . Following initial determination of the scale factor, data sets were scaled using a simple FORTRAN program that allowed K to be set manually. The B-factor determined by XSCALE was ignored in this manual scaling procedure as this additional resolution-dependent scale factor does not have a large effect at low resolution.

A series of difference-intensity “data sets” was calculated from the same derivative and native data sets to 7Å resolution. In each case, a different scale factor (less than or greater than the initial estimate) was applied. These sets of difference-intensity values were calculated by subtracting the native intensity from the scaled derivative intensity for each reflection ( $(K \cdot I_{\text{der}}) - (I_{\text{nat}})$ ).

Pseudo-precession-like plots of difference intensities were displayed with a modified version of RECIP, a reciprocal-space display program (G.N. Phillips). Intensity-weighted

positive and negative differences were displayed in contrasting colors so as to highlight the effects of the mercury compound on the intensity distribution. The strongest positive and negative differences were given a value for the maximum red and blue intensity respectively in a color table that was determined independently for each plot. The range of positive and negative differences was then each fit to a straight line with slopes such that the intensity of the red and blue pixel values decreased to zero (black) at a variable threshold value and the largest differences were assigned the maximum intensity (255) of red or blue pixels.

The sublattice analysis was restricted to finding the positions of the mercury atom pairs at 7Å resolution. The pairs were each modeled as a point scatterer, a small, uniform B-factor was applied, and XPLOR<sup>49</sup> was used to calculate the transform of several arrangements. Pseudoprecession-like plots were then made of the resulting calculated structure factor amplitudes. Simulated difference Patterson maps were made from calculated intensities of the point scatterer model.

The mercury-pair positions were refined independently at 7Å resolution with the crystallographic analysis packages Xtalview and Phases.<sup>50,51</sup> The data sets were pre-scaled according to the qualitative analysis, and the scale factor between the data sets was not refined. The sites refined to approximately equal occupancy and provided good phasing power (1.685 at 7.0Å resolution from Xtalview). SIR refinement was not improved by including anisotropic B-factors. The Phases package was used to assimilate the anomalous difference data and the SIR solution in a SIRAS (SIR + Anomalous Scattering) phase refinement and to perform solvent flattening and phase combination.

QUANTA was used to build an atomic model, using the GCN4 coiled-coil structure as a template. The positions of the molecular ends were determined relative to the Cys-190 residues, whose positions were fixed by the solution of the mercury-pair positions. The sequence of tropomyosin was then imposed on the model and the side-chain positions were regularized with QUANTA. Two alternative antiparallel model structures (antiparallel choices 1 and 2) and alternative parallel models (parallel choices 1 and 2) were constructed in this way. In each case, the ends of the molecules were also modeled as ideal coiled coil and overlapped by about 10 residues. The terminal segments were each placed slightly to the side of the overall run of the filaments, creating a crude 4-helix bundle at the end-to-end overlap.

Positional refinement was carried out with XPLOR in order to anneal the segments of the antiparallel choice-1 together and form a single filament. Distances were determined from the GCN4 structure for the separation of the  $\alpha$ -carbon atoms of all *a* and *d* position residues. The average *a*-to-*a* and *d*-to-*d* carbon- $\alpha$  distances calculated from the GCN4 structure are 5.65Å (standard deviation = 0.17Å) and 6.28Å (standard deviation = 0.12Å), respectively. These distances were included as NOE restraints to hold the two  $\alpha$  helices in a reasonable coiled-coil conforma-

tion. The energy associated with these distances was scaled relative to other geometric factors so as to force the molecule to assume this ideal coiled-coil geometry. In addition, following positional refinement, incremental adjustments of 2, 4, and 7Å were made in the position of the ends of the molecules by "sliding" the sequence of each molecule in both directions along the path of the filament, maintaining the proper azimuthal relationship of the helices to one another. After each axial movement, the structure was re-refined. Coordinates have been deposited at the Protein Data Bank (accession code 1C1G).

## ACKNOWLEDGMENTS

We thank Anand Kolatkar, Mike Quillin, and Mitch Miller for help throughout. We are grateful to Steve Ginell, Lisa Keefe, and Jim Pflugrath for help with data collection at BNL and to Henry Bellamy for data collection at SSRL. We also thank Bill Weis for help with the attempt at MAD phasing.

## REFERENCES

1. Harbury PB, Zhang T, Kim PS, Alber T. A switch between two-, three-, and four-stranded coiled coils in GCN4 leucine zipper mutants. *Science* 1993;262:1401–1406.
2. McLachlan AD, Stewart M. Tropomyosin coiled-coil interactions: evidence for an unstaggered structure. *J Mol Biol* 1975;98:293–304.
3. Parry DAD. Analysis of the primary sequence of  $\alpha$ -tropomyosin from rabbit skeletal muscle. *J Mol Biol* 1975;98:519–535.
4. Stone D, Sodek J, Johnson P, Smillie LB. Tropomyosin: correlation of amino acid sequence and structure. In *Proteins of contractile systems*, Vol. 31. Amsterdam: North Holland Publishing; 1976. p 125–136.
5. Cohen C, Holmes KC. X-ray diffraction evidence for alpha-helical coiled coils in native muscle. *J Mol Biol* 1963;6:423–432.
6. Crick FHC. The packing of alpha-helices: simple coiled-coils. *Acta Cryst* 1953;6:689–697.
7. McLachlan AD, Stewart M. The 14-fold periodicity in alpha-tropomyosin and the interaction with actin. *J Mol Biol* 1976;103:271–298.
8. Phillips GN Jr, Fillers JP, Cohen C. Tropomyosin crystal structure and muscle regulation. *J Mol Biol* 1986;192:111–131.
9. Hitchcock-DeGregori SE. Structural requirements of tropomyosin for binding to filamentous actin. *Adv Exp Med Biol* 1994;358:85–96.
10. Hitchcock-DeGregori SE, Varnell TA. Tropomyosin has discrete actin-binding sites with sevenfold and fourteenfold periodicities. *J Mol Biol* 1990;214:885–896.
11. Kress M, Huxley HE, Faruqi AR, Hendrix J. Structural changes during activation of frog muscle studied by time-resolved X-ray diffraction. *J Mol Biol* 1986;188:325–342.
12. Bivin DB, Stone DB, Schneider DK, Mendelson RA. Cross-helix separation of tropomyosin molecules in acto-tropomyosin as determined by neutron scattering. *Biophys J* 1991;59:880–888.
13. Chacko S, Phillips GN Jr. Diffuse X-ray scattering from tropomyosin crystals. *Biophys J* 1992;61:1256–1266.
14. Phillips GN Jr, Chacko S. Mechanical properties of tropomyosin and implications for muscle regulation. *Polymers* 1996;38:89–95.
15. Lehman W, Craig R, Vibert P. Calcium-induced tropomyosin movements in limulus thin filaments revealed by three-dimensional reconstruction. *Nature* 1994;368:65–67.
16. Lehman W, Vibert P, Ulman P, Craig R. Steric-Blocking by Tropomyosin Visualized in Relaxed Vertebrate Muscle Thin Filaments. *J Mol Biol* 1995;251:191–196.
17. Lorenz M, Poole KJ, Popp D, Rosenbaum G, Holmes KC. An atomic model of the unregulated thin filament obtained by X-ray fiber diffraction on oriented actin-tropomyosin gels. *J Mol Biol* 1995;246:108–119.

18. Zou G, Phillips GN Jr. A cellular automation model for the regulatory behavior of muscle thin filaments. *Biophys J* 1994;67:11–28.
19. Crick FHC. Is alpha-keratin a coiled coil? *Nature* 1952;170:882–883.
20. Phillips GN Jr, Lattman EE, Cummins P, Lee KY, Cohen C. Crystal structure and molecular interactions of tropomyosin. *Nature* 1979;278:413–417.
21. Phillips GN Jr, Cohen C, Stewart M. A new crystal form of tropomyosin. *J Mol Biol* 1987;195:219–223.
22. Whitby FG, Kent H, Stewart F, et al. Structure of tropomyosin at 9 Ångströms resolution. *J Mol Biol* 1992;227:441–452.
23. Phillips GN Jr. What is the pitch of the alpha-helical coiled coil? *Proteins* 1992;14:425–429.
24. Hvidt S, Nestler HM, Greaser ML, Ferry JD. Flexibility of myosin rod determined from dilute solution viscoelastic measurements. *Biochemistry* 1982;21:4064–4073.
25. Stewart M, McLachlan AD, Calladine CR. A model to account for the elastic element in muscle crossbridges in terms of a bending myosin rod. *Proc Roy Soc Lond* 1987;B229:381–413.
26. Nilges M, Brunger AT. Automated modeling of coiled coils: application to the GCN4 dimerization region. *Prot Engineer* 1991;4:649–659.
27. Nilges M, Brunger AT. Successful prediction of the coiled coil geometry of the GCN4 leucine zipper domain by simulated annealing: comparison to the X-ray structure. *Proteins* 1993;15:133–146.
28. O'Shea EK, Klemm JD, Kim PS, Alber T. X-ray structure of the GCN4 leucine zipper, a two-stranded parallel coiled coil. *Science* 1991;254:539–544.
29. Saudek V, Pastore A, Castiglione-Morelli MA, Frank R, Gausepohl H, Gibson T. The solution structure of a leucine-zipper motif peptide. *Prot Engineer* 1991;4:519–529.
30. Saudek V, Pastore A, Castiglione-Morelli MA, et al. solution structure of the DNA-binding domain of the yeast transcriptional activator protein GCN4. *Prot Engineer* 1990;4:3–10.
31. Casper DLD, Cohen C, Longley W. Tropomyosin: crystal structure, polymorphism and molecular interactions. *J Mol Biol* 1969;41:87–107.
32. Cohen C, Longley W. Tropomyosin paracrystals formed by divalent cations. *Science* 1966;152:794–796.
33. Stewart M. Tropomyosin: evidence for no stagger between chains. *FEBS* 1975b;53:5–7.
34. Stewart M. Structure of  $\alpha$ -tropomyosin magnesium paracrystals. *J Mol Biol* 1981;148:411–425.
35. Stewart M, Diakiv V. Electron microscopic location of protein thiol residues. *Nature* 1978;274:184–186.
36. Stewart M, Lepault J. Cryoelectron microscopy of tropomyosin magnesium paracrystals. *J Microscopy Pt. 1*, 1985;138:53–60.
37. Stewart M, McLachlan AD. Fourteen actin binding sites on tropomyosin? *Nature* 1975;257:331–333.
38. Stewart M, McLachlan AD. Structure of magnesium paracrystals of tropomyosin. *J Mol Biol* 1976;103:251–269.
39. Avila-Sakar AJ, Schmid MF, Li L, Whitby FG, Phillips GN Jr, Chiu W. Preliminary electron crystallographic analysis of ice-embedded tropomyosin crystals. *J Struct Biol* 1993;110:67–74.
40. Xie X, Sudhakara R, Walian P, Hatch V, Phillips GN Jr, Cohen C. Coiled-coil packing in spermine-induced tropomyosin crystals: a comparative study of three forms. *J Mol Biol* 1994;236:1212–1226.
41. Hitchcock-DeGregori SE, Heald RW. Altered actin and troponin binding of amino-terminal variants of chicken striated muscle alpha-tropomyosin expressed in *Escherichia coli*. *J Biol Chem* 1987;262:9730–9735.
42. Lees-Miller JP, Helfman DM. The molecular basis for tropomyosin isoform diversity. *BioEssays* 1991;13:429–437.
43. Pittenger MF, Kazzaz JA, Helfman DM. Functional properties of non-muscle tropomyosin isoforms. *Curr Opin Cell Biol* 1994;6:96–104.
44. Eisenberg E, Kielley WW. Troponin-tropomyosin complex. *J Biol Chem* 1974;249:4742–4748.
45. Phillips GN Jr. Crystallization in capillary tubes. *Methods Enzymol* 1985;114:128–131.
46. Stewart M. The location of the troponin binding site on tropomyosin. *Proc R Soc London Ser B*, 1975a;190:257–266.
47. Kabsch W. Evaluation of single-crystal X-ray diffraction data from a position-sensitive detector. *J Appl Cryst* 1988;21:916–924.
48. Hendrickson WA, Smith JL, Phizackerly RP, Merritt EA. Crystallographic structure analysis of lamprey hemoglobin from anomalous dispersion of synchrotron radiation. *Proteins* 1988;4:77–88.
49. Brunger AT, Kuriyan J, Karplus M. Crystallographic R-factor refinement by molecular dynamics. *Science* 1987;235:458–460.
50. Furey W, Swaminathan S. PHASES: a program package for the processing and analysis of diffraction data from macromolecules. American Crystallographic Association meeting abstracts, 1990; 18:73.
51. McRee DE. A visual protein crystallographic software system for X11/XView. *J Mol Graphics* 1992;10:44–46.